Letter

Nano-optical Imaging of In-Plane Homojunctions in Graphene and MoS$_2$ van der Waals Heterostructures on Talc and SiO$_2$

Andreij C. Gadelha, Thiago L. Vasconcelos, Luiz G. Cançado, and Ado Jorio*
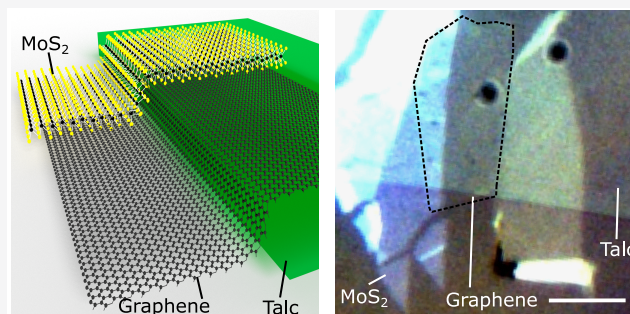
Read Online

ACCESS | Metrics & More | Article Recommendations

ABSTRACT: Understanding the impact of doping variations on the physical properties of two-dimensional materials is important for their application in electronic and optoelectronic devices. Here we report a nano-optical study on graphene and MoS$_2$ homojunctions by placing these two materials partly on top of a layered talc substrate, partly on top of an SiO$_2$ substrate. By analyzing the nano-Raman scattering from graphene and the nanophotoluminescence emission from MoS$_2$, two different doping zones are evident with sub-100 nm wide charge oscillations. The oscillations occur abruptly at the homojuction and extend over longer distances away from the interface, indicating imperfect deposition of the two-dimensional layer on the substrate. These results evidence fine and unexpected details of the homojuctions, important to build better electronic and optoelectronic devices.

The versatile two-dimensional (2D) van der Waals heterostructures compose an important platform for the development of ultrathin and flexible electronic and optoelectronic devices.[1−6] More specifically, graphene and MoS$_2$ can generate wide bandwidth and highly efficient photodetectors and light-emitting devices,[7,8] valley-spin polarized emitters and absorbers,[9] photothermoelectric,[10] and photomemory devices.[11] Besides the specific combination of properties within a heterostructure,[3] the key aspect of these 2D material devices are their junctions, which can be out-of-plane[12] or in-plane.[12−15] The most commonly applied is the in-plane type, named as homojuction, in which a single material is utilized.

Optical spectroscopy involves a variety of nondestructive techniques able to extract a wide range of spectroscopic information from material systems. However, the spatial resolution is usually limited to the micrometer-scale due to light diffraction. The use of nanoantennas to enhance and detect the near-field interactions has been employed to overcome the diffraction limit and to attempt to image p−n junctions in bulk semiconductors.[16−18] More recently, some works reported imaging of MoS$_2$−WS$_2$ lateral heterojunctions with submicron resolution, but lacking in-depth spectroscopic analysis.[19,20] The problem is that the nanoantenna strategies, such as tip-enhanced Raman scattering (TERS)[21−24] or tip-enhanced photoluminescence (TEPL)[24,25] are generally efficient for locally enhancing the optical signal from zero- or one-dimensional features, being hardly effective to study the intrinsic properties of two-dimensional systems. The reason for that lies in the competition between the locally enhanced signal from the tip apex vicinity and the large area originating

the far-field emission,[26−28] thus hindering the observation of subtle intrinsic details in 2D materials.

Here we report a robust nanospectroscopy study of homojuctions that was possible due to a high-optically efficient tip-enhanced system, which enables measuring local variations in the intrinsic properties of the two-dimensional structures.[29−33] We developed lateral homojunctions by depositing a 2D layer partly on top of a thin (∼30 nm thick) layered talc[34,35] and partly on top of a SiO$_2$ substrate (see Figure 1a). Graphite, MoS$_2$, and talc crystals were exfoliated with a blue tape and transferred into a SiO$_2$/Si wafer. Both graphene and MoS$_2$ flakes were optically selected and transferred atop the talc flake by the pick-up method described in ref 36. Talc was demonstrated to generate a spontaneous p doping,[37] and the two different homojunctions are made one of graphene and the other of MoS$_2$, talc removing electrons in both materials, creating two regions of different doping: graphene (MoS$_2$) on talc and graphene (MoS$_2$) on SiO$_2$.

Figure 1b exhibits an optical micrograph of the heterostructure, where the optically faint monolayer graphene is highlighted by the dashed line. Figure 1c presents a micro-PL map from MoS$_2$, where an enhancement of the PL signal on
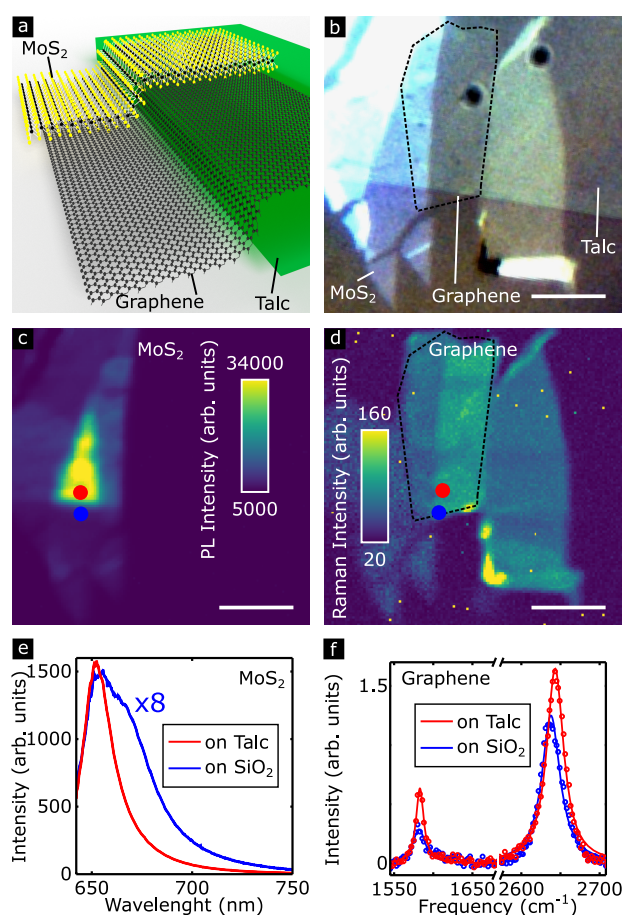
Figure 1. Micro-optical characterization of the heterostructure. (a) Sketch of the heterostructure. (b) Bright-field optical image of the heterostructure. (c) Photoluminescence (PL) map of MoS_2. (d) Raman map of the graphene's 2D band. (e) PL spectra of MoS_2 on talc (red) and on SiO_2 (blue). (f) Raman spectra of graphene on talc (red) and on SiO_2 (blue). All images were obtained with a Nikon Eclipse Ti−U inverted microscope equipped with a 60× and 1.4 NA objective lens. Raman and PL were excited with a HeNe (632.8 nm) laser, 750 μW power at the sample, recorded using an Andor spectrometer equipped with an iDus DU401A-BR-DD charged-coupled device (CCD). The scale bars in panels b−d indicate 20 μm.

talc can be clearly observed. Figure 1d shows a micro-Raman map of graphene recorded from the intensity of the 2D band (also named G' in the literature, at 2650 cm^{-1}). There is no clear variation of the graphene's 2D band intensity in Figure 1d, but a background PL emission from the MoS_2 monolayer. Figure 1e plots the MoS_2 PL spectrum recorded on talc (red), and on SiO_2 (blue). On talc, the MoS_2 PL is more intense than on SiO_2 and the PL spectral shape changes significantly. The two regions (in and out talc) also render different spectral characteristics of the graphene Raman peaks, as shown in Figure 1f, where one can see the G ($\sim$1583 cm^{-1}) and 2D Raman peaks. In the following we investigate these effects, which are interestingly modulated at the nanoscale homojuctions.

Starting with the graphene homojunction, Figure 2 presents a nano-Raman investigation[28] of graphene@talc/graphene@ SiO_2 junction down to a 10 nm resolution, performed at ambient conditions. The nano-optics system is a combination of a micro-Raman and a scanning probe microscopy setups in a TERS configuration, as described in ref 30. The highly efficient

nanoantennas are monopole-based plasmon-tunable tip pyramids.[29,31] Figure 2a shows an atomic force microscopy (AFM) topography image of the junction graphene@talc/ graphene@SiO_2 where, at the bottom of the panel, the graphene is on top of talc (yellow-shaded), and at the top of the panel, the graphene is on top of SiO_2. Panels b−d of Figure 2 present the Raman spectral maps at the same location as in Figure 2a, drawn using the 2D band's intensity, frequency, and full-width at half-maximum (FWHM), respectively. A broader area was originally measured, but because of tip drifting and lost of enhancement, only part of the measurement is shown here. As shown in Figure 2b, the 2D intensity is similar on top talc and SiO_2, but there are abrupt changes when crossing the homojunction interface. The intensity variation along the homojunction is due to the loss of near-field enhancement caused by tip drift in respect to the center of the laser focus. Figure 2c depicts higher 2D frequencies for graphene@talc relative to graphene@SiO_2, with frequency nanoscale oscillations at the interface. Figure 2d depicts a 2D peak broadening at the interface.

Figure 2e (both panels) plots the (same) averaged topography profile across the junction, with the vertical dashed lines indicating the $\sim$60 nm wide transition from talk to SiO_2. Graphene@talc appears on the left (lateral distances <290 nm), where the topography is higher, and graphene@SiO_2 is on the right side (lateral distances >350 nm). We measured a $\sim$30 nm step (the talc thickness) across the heterostructure, and we use the topography profile to mark the junction location at the other panels using the red-dashed lines. Panels f−h of Figure 2 show the across-junction average behavior of the Raman peak intensities, frequencies, and FWHMs, respectively, for the 2D (left graphics) and G (right graphics) bands. Focusing initially on the 2D band (left panels), the intensity nano-oscillations in Figure 2f display a local maximum at 300 nm, followed by global minimum at 330 nm. Within the SiO_2 substrate, the 2D intensity exhibits oscillations also seen in Figure 2b. The 2D frequency in Figure 2g shows a 15 cm^{-1} decrease when crossing the interface, and oscillations with frequency maxima coinciding with the 2D intensity minima in Figure 2f. Finally, the FWHM plot in Figure 2h confirms a broadening of the 2D mode at the interface. The G profiles (right panels) are noisier because of the intrinsic lower intensity (lower signal-to-noise ratio), but one can see that it shows similar results as observed for the 2D band. The oscillations at the SiO_2 side may be due to wrinkles caused by the graphene deposition, consistent with the faint topography variations at the SiO_2 side in Figure 2e.

The variations of the graphene Raman peaks can have origin in several physical mechanisms such as strain, doping, and electron−phonon coupling.[38,39] Therefore, we should employ alternative methods to distinguish between these mechanisms. Here, we draw our attention to the strain and doping aspects. The method introduced by Lee et al. separates the influence of doping and strain[40] by plotting the 2D vs G band frequencies; a pure strain gives a data distribution over a 2.2 slope line, while pure doping over a 0.75 slope line. Moreover, Neumann et al. shows that FWHM plots also translate nanometer-scale strain variations over a 2.2 slope line.[41] Figure 3a thus presents frequency plots of the 2D vs G bands recorded at (blue dots) and outside (black dots) the interface. The 2.2 (red) and 0.75 (black) slope lines are arbitrarily plotted near the data for reference. The black dots exhibit two majority data sets whose center of mass fall into the 2.2 slope line. However, the data of
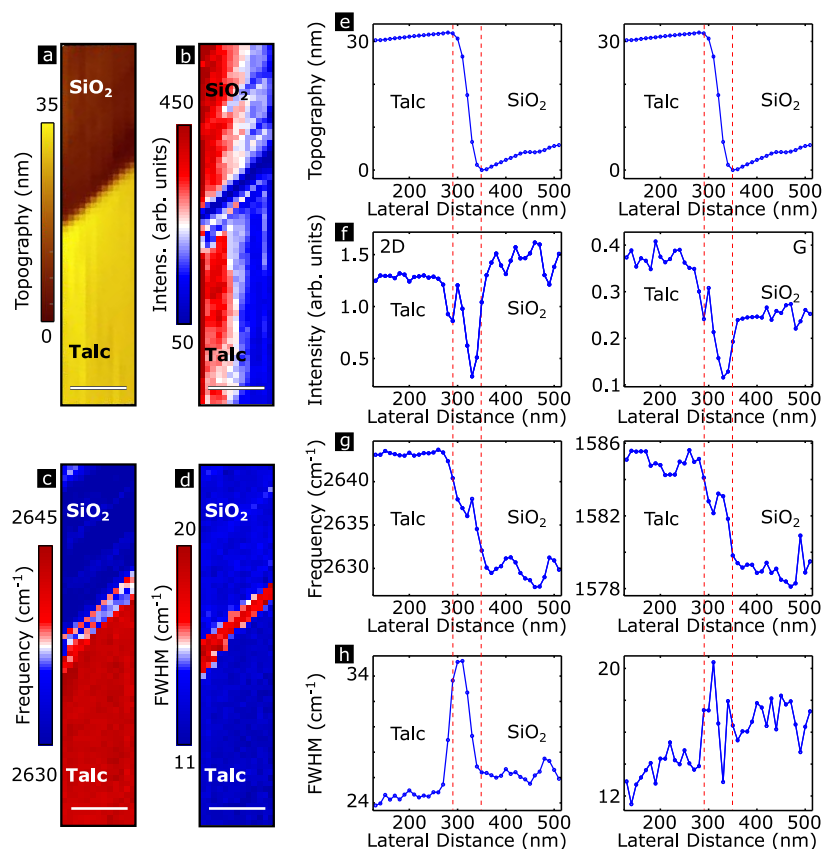
Figure 2. Nano-Raman characterization of the graphene@talc/graphene@SiO$_2$ hetereostructure. (a) AFM topography image of the graphene@talc/graphene@SiO$_2$ hetereostructure. (b−d) Simultaneously obtained nano-Raman maps of the intensity, frequency, and FWHM of the graphene's 2D band, respectively. The scale bars in panels a−d are 100 nm. (e) Topography profile across the junction. (f−h) Raman intensities, frequencies, and FWHM, respectively, for the graphene 2D (left panels) and G (right panels) bands. The data in panels e−h are an average over all the vertical line profiles across the junction in panels a−d, after accounting for the slope in the junction position. For the nano-Raman measurements we use a laser power of 200 μW and 1 s accumulation time per pixel.

each one of the two data sets scatters in a mixture between 2.2 and 0.75 slope lines. The data at the interface (blue dots) transit from the two observed distributions outside the interface. By inspecting the FWHM plot in Figure 3b, no clear trend can be observed, except for a clear spread of the interface region. Hence, from the above analyses we conclude that doping plays a major role in the difference between the two regions (graphene@talc and graphene@SiO$_2$); i.e., overall, the observed effects might be due to a mixture of both with prevailing doping.

Das et al. demonstrated that the intensity ratio between the 2D and G peaks is inversely proportional to the charge doping (for doping values lower than ∼10^{13} cm^{-2}).[42] To check this viewpoint, an intensity ratio (I_{2D}/I_G) map is shown in Figure 3c, and an averaged line profile is provided in Figure 3d. At the talc region, lower I_{2D}/I_G is observed, which corresponds to a higher doping,[42] while a lower doping is evidenced at the SiO$_2$ side (high I_{2D}/I_G). Compellingly, we observe an abrupt I_{2D}/I_G oscillation close to the interface, a peak followed by a dip at the interface, consistent with results in Figure 2, and noisy oscillations elsewhere.

We cannot quantitatively estimate the carrier concentration through the I_{2D}/I_G parameter in Figure 3d, because ref 42 works on the far-field regime, while we explore the nearfield, where the 2D and G bands are amplified distinctively.[43,44] However, we can use the intensity ratio as a qualitative indicator. Moreover, ref 37 reports that talc provides a

spontaneous p-doping in graphene of the order of ∼10^{13} cm^{-2}. Graphene devices on SiO$_2$ are slightly p-doped, with a ∼10^{12} cm^{-2} carrier concentration.[45] Thus, we expect that these differently doped regions generate a p−p′ junction at the interface (with p′ < p). The graphene doping monotonically varies from higher doped p to a lighter doped p′. However, Figure 3d shows an abrupt change of heavier-doping p at talc, to moderate doping at the interface, then to a more doped condition again after the interface, and finally to lower-doped p′ at SiO$_2$. Thus, the graphene heterostructure forms a pp′pp′ junction (see Figure 3d). We also depict on the top panel of Figure 3d a sketch of the graphene charge neutral point (CNP) over the junction. This oscillation is surprising, and we could not explain how talc induces these effects. We hope these results will encourage theorists to model this system.

Moving now to the MoS$_2$ device, conversely to graphene, this 2D material is a direct band gap semiconductor, whose optical properties are pronounced by tightly bound neutral and charged (trion) excitons.[46] Mak et al. showed that the energy difference ($\omega_A − \omega_{A^-}$) between the energies of the neutral (A) and negatively charged (A-) excitons is directly proportional to the MoS$_2$ Fermi level, and increases monotonically with doping due to the combined effects of Pauli blocking and many-body interactions.[47] Thus, we plot in Figure 4a a map of $\omega_A − \omega_{A^-}$ recorded from the MoS$_2$ nano-PL, on the right, and an AFM topography map on the left, with a consistent talc thikess of ∼30 nm (see Figure 5a). We also indicate the
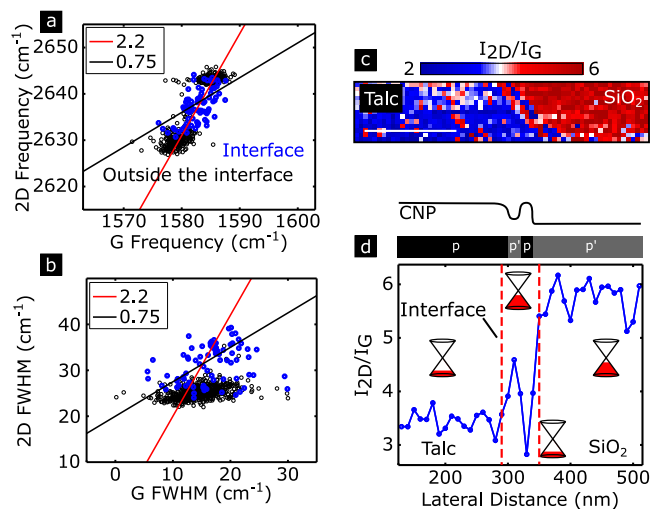
Figure 3. Graphene nano-Raman data analisis. (a) 2D vs G band frequency plot at the graphene@talc/graphene@SiO₂ hetereostructure. (b) 2D vs G band FWHM plot equivalent to (a). The black dots are data from the area outside the interface, whereas the blue dots are data at the interface. In panels a and b we plot arbitrary lines with 2.2 (red) and 0.75 (blue) slopes. (c) I_{2D}/I_G Raman map recorded at the graphene@talc/graphene@SiO₂ heterostructure. The scale bar is 200 nm. (d) The botton panel is a I_{2D}/I_G averaged line profile and the top panel is an illustration of the charge neutral point (CNP) over the junction. A laser power of 200 μW was used for these measurements.

interface region in Figure 4a with a black-dot-dashed line. The original measurement suffered from tip drifts during the image acquisition, and for a better visualization of the effects we fixed this drift manually, by adjusting the relative position of the image lines without compromising the information contained in the data set. The right panel of Figure 4a displays low values of $\omega_A - \omega_{A^-}$ at talc (bottom) and higher values at SiO₂ (top).

Similar to the case of graphene, at the interface we observe oscillations of $\omega_A - \omega_{A^-}$, which are extended at longer distances within the SiO₂ substrate (see Figure 4a). To deeply explore the spectral variations, in Figures 4b−e the PL spectra at regions indicated by arrows in Figure 4a are shown. Two Lorentzians are used to fit the neutral and charged exciton PL contributions. Besides, we plot in Figure 4f an averaged line profile over four lines from the yellow dashed box at Figure 4a (right) showing $\omega_A - \omega_{A^-}$ on the left axis, and E_F on the right axis, according to the phenomenological relation described by the equation (in meV unit):[47]

$$\omega_A - \omega_{A^-} = 1.2 \times E_F + 18 \qquad (1)$$

Therefore, assuming that the oscillations at the interface on Figure 4f are due to doping, we evaluate E_F from $\omega_A - \omega_{A^-}$ according to eq 1. Note that E_F varies from 10 meV on talc to 30 meV at the interface, moving abruptly to 10 meV, and then back to 30 meV on SiO₂. This behavior is similar to what we observe in graphene (see Figure 3d), but here we measure a n′n n′n junction (n > n′), reflecting a global localized doping dynamics effect. The top panel in Figure 4f exhibits a schematic illustration of the MoS₂ band structure across the junction. Since MoS₂ is a semiconductor, the particular configuration in Figure 4f allows localized potential wells that can confine excitons. Furthermore, oscillations of $\omega_A - \omega_{A^-}$ at the SiO₂ side are now clearly observed (while the oscillations of the 2D and G graphene features were faint in
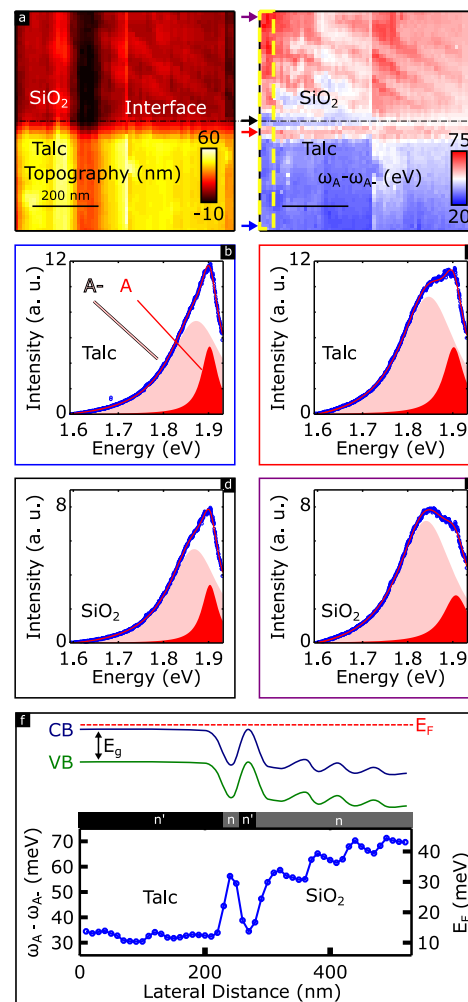
Figure 4. Nano-PL of MoS₂@talc/MoS₂@SiO₂. (a) Topography map on the left, and $\omega_A - \omega_{A^-}$ map recorded from the MoS₂ nano-PL on the right. (b−e) Nano-PL spectra recorded from the areas indicated by the arrows in panel a (see colors for each location). Two Lorentizans with all parameters free are used to fit the PL spectra. (f) The bottom panel depicts the experimentally obtained $\omega_A - \omega_{A^-}$ (left axis) and the converted E_F averaged value (right axis, according to eq 1). The top panel illustrates the energy structure across the junction. For these measurements we used a laser power of 200 μW and 1 s accumulation time per pixel. A long-pass filter (Razor edge Long Pass 633 nm) is utilized to remove the 632.8 nm laser excitation (1.96 eV), which is close to the exciton energy ($\lesssim$1.9 eV).

SiO₂), also visible in Figure 4f, that might be related to strain, since they are also visible in the topography shown Figure 4a.

Figure 5 presents a more detailed nanospectroscopy analysis of the MoS₂ data. The averaged AFM topography of the junction in shown in Figure 5a (the left and right panels are the same measurement). Panels b−d of Figure 4 plot the energy, FWHM, and PL intensity, respectively, for the neutral (at left) and charged (trion, at right) excitons. These profiles are the result of the average over the four lines delimited by the yellow rectangle on the right panel of Figure 4a. In Figure 5 we delimit the interface with the dashed black lines. In Figure 5b we observe clear oscillations of the trion energy (A-, right), absent in the neutral exciton (A, left). We observe the FWHM oscillation in Figure 5c is similar for both neutral exciton and trion at the interface, but the oscillations on the SiO₂ are more evident for the neutral exciton. The PL intensity also depicts
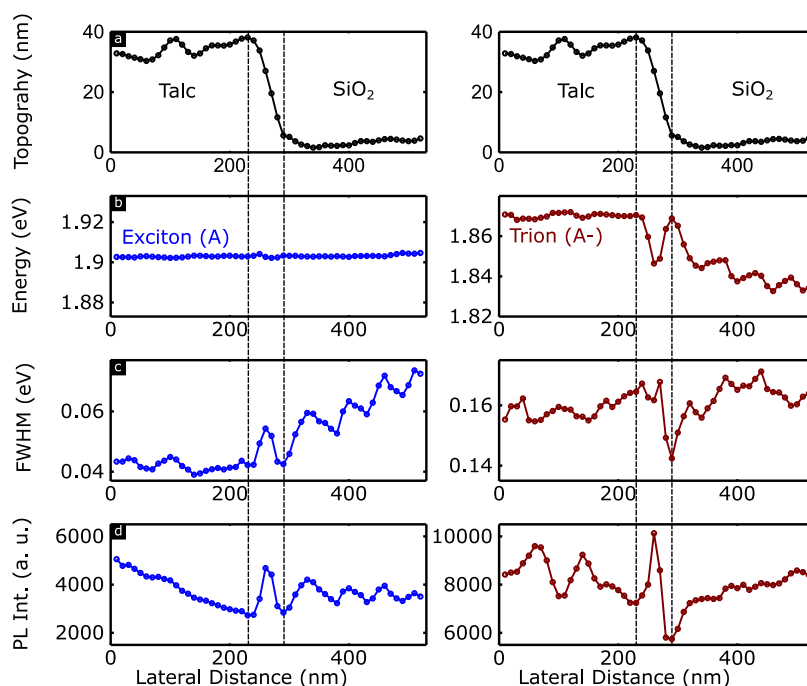
Figure 5. Nanospectroscopy profile analysis of junctions in MoS$_2$@talc/MoS$_2$@SiO$_2$. (a) Topography profile. (b−d) Energy, FWHM, and PL intensity profiles, respectively, for the neutral exciton (A), on the left, and for the trion (A-), on the right. To generate the line profiles above, the four lines delimited by a dashed yellow rectangle on the right panel of Figure 4a were averaged.

strong oscillations for both neutral exciton and trion, and again they show similar results at the interface, and the oscillations on the SiO$_2$ side is discernible for the neutral exciton.

Reference 48 shows that the neutral exciton and trion energies of a strained monolayer MoS$_2$ suffers a red shift with the applied strain with similar magnitudes. Contrarily, the magnitude of the energy oscillation of the trion in Figure 5b is higher than the neutral exciton. So, only the strain seems not to be sufficient to account for the oscillations in Figure 5b. Another circumstance is that, at the middle of the edge (where a strong strain would be expected), we observe an intensity peak of the neutral exciton in Figure 5d. A strained MoS$_2$ has a PL quenching, in contrast to our result. Again, our results suggest that only strain cannot describe our results, and the charge doping might have a significant contribution. We also note that the energy variation of the trion is higher than the neutral exciton in Figure 5b, which is a unusual behavior when compared to ref 47. It is worth investigating further to elucidate these substrate interactions. These results are consistent with local strain-doping effects, as discussed for p−i−n junction,[49] strain-induced one-dimensional moiré potentials[50] and strain soliton networks.[51] Other than that, the oscillations of the FWHM, Figure 5c, are also interesting and may be due to lifetime variations across the junction that should be investigated in future works.

Finally, it is interesting to compare the results reported here with the previous development of a lateral homojunction by substrate dielectric engineering.[52] Utama et al. created an MoS$_2$ junction based on the band gap variations using substrates whose dielectric constant differs by about a factor of 3. In our case, talc has dielectric constants observed to range between 2 and 4.7,[37] while SiO$_2$ has a well-established dielectric constant of 3.9. Therefore, the difference to be considered here is much smaller when compared to the ones utilized by Utama et al. Indeed, the MoS$_2$ band gap

discrepancy in talc and SiO$_2$ seems to be smaller than 10 meV (see left panel in Figure 5b), while in ref 52 the authors claim to achieve 180 meV. Based on these differences and on the experimental evidence for doping we discussed here, we believe our results are mostly due to doping variations caused by Fe or Al acceptor impurities replacing Si sites in talc, removing electrons from the graphene and MoS$_2$ layers deposited on it (see also ref 37).

In summary, direct visualization of lateral homojunctions show spectral oscillations in the tens-of-nanometers scale. To achieve these results, we employed a highly efficient near-field optics setup and built a heterostructure of monolayer graphene and MoS$_2$ side-by-side and precisely placed part on talc and a part on SiO$_2$. In graphene, we observed oscillations of the 2D and G bands intensities and frequencies, and a broadening of these peaks at the junction. By inspecting the 2D/G intensity ratio at the junction, we confirmed that local doping variations across the junctions explain these oscillations. For MoS$_2$, we showed that the energy difference between the neutral and charged exciton follows a similar trend, pointing to a doping oscillation at the junction, similarly to what we observed in graphene. Furthermore, the observed oscillations extend to the lower topograpy (SiO$_2$) of the device, which might indicate imperfection when depositing the 2D layers in this heterosubstrate. Our work helps understanding the fine details of the homojuctions, important to build better electronic and optoelectronic devices.

■ AUTHOR INFORMATION

Corresponding Author

Ado Jorio − *Physics Department, Universidade Federal de Minas Gerais, Belo Horizonte, MG 31270-901, Brazil; Electrical Engineering Graduate Program, Universidade Federal de Minas Gerais, Belo Horizonte, MG 31270-901,*

Brazil; ● orcid.org/0000-0002-5978-2735;
Email: adojorio@fisica.ufmg.br

Authors

Andreij C. Gadelha − *Physics Department, Universidade Federal de Minas Gerais, Belo Horizonte, MG 31270-901, Brazil; Department of Physics, Department of Chemistry, and JILA, University of Colorado at Boulder, Boulder, Colorado 80309, United States;* ● orcid.org/0000-0002-6350-7680

Thiago L. Vasconcelos − *Instituto Nacional de Metrologia, Qualidade e Tecnologia (Inmetro), Duque de Caxias, RJ 25250-020, Brazil*

Luiz G. Cançado − *Physics Department, Universidade Federal de Minas Gerais, Belo Horizonte, MG 31270-901, Brazil;* ● orcid.org/0000-0003-0816-0888

Complete contact information is available at:
https://pubs.acs.org/10.1021/acs.jpclett.1c01804

Author Contributions

Sample preparation: Andreij C. Gadelha. Plasmonic nano-antenna: Thiago L. Vasconcelos. Nano-Raman and nano-PL measurements: Andreij C. Gadelha. Data Analysis: Andreij C. Gadelha and Ado Jorio. Project idealization and guidance: Ado Jorio, Andreij C. Gadelha, and Luiz G. Cançado. Paper writing: Ado Jorio, Andreij C. Gadelha, Luiz G. Cançado, and Thiago L. Vasconcelos.

Notes

The authors declare no competing financial interest.
The experimental data related to this work can be obtained upon request to the contact authors.

■ REFERENCES

(1) Wang, J.; Mu, X.; Sun, M.; Mu, T. Optoelectronic properties and applications of graphene-based hybrid nanomaterials and van der Waals heterostructures. *Applied Materials Today* **2019**, *16*, 1−20.

(2) Bonaccorso, F.; Sun, Z.; Hasan, T.; Ferrari, A. C. Graphene photonics and optoelectronics. *Nat. Photonics* **2010**, *4*, 611−622.

(3) Frisenda, R.; Molina-Mendoza, A. J.; Mueller, T.; Castellanos-Gomez, A.; van der Zant, H. S. J. Atomically thin p−n junctions based on two-dimensional materials. *Chem. Soc. Rev.* **2018**, *47*, 3339−3358.

(4) Rossi, A.; Spirito, D.; Bianco, F.; Forti, S.; Fabbri, F.; Büch, H.; Tredicucci, A.; Krahne, R.; Coletti, C. Patterned tungsten disulfide/graphene heterostructures for efficient multifunctional optoelectronic devices. *Nanoscale* **2018**, *10*, 4332−4338.

(5) Li, D.; Chen, M.; Sun, Z.; Yu, P.; Liu, Z.; Ajayan, P. M.; Zhang, Z. Two-dimensional non-volatile programmable p−n junctions. *Nat. Nanotechnol.* **2017**, *12*, 901.

(6) Withers, F.; Del Pozo-Zamudio, O.; Mishchenko, A.; Rooney, A. P.; Gholinia, A.; Watanabe, K.; Taniguchi, T.; Haigh, S. J.; Geim, A. K.; Tartakovskii, A. I.; Novoselov, K. S. Light-emitting diodes by band-structure engineering in van der Waals heterostructures. *Nat. Mater.* **2015**, *14*, 301−306.

(7) De Sanctis, A.; Jones, G. F.; Wehenkel, D. J.; Bezares, F.; Koppens, F. H. L.; Craciun, M. F.; Russo, S. Extraordinary linear dynamic range in laser-defined functionalized graphene photo-detectors. *Science Advances* **2017**, *3*, e1602617.

(8) Thakar, K.; Lodha, S. Optoelectronic and photonic devices based on transition metal dichalcogenides. *Mater. Res. Express* **2020**, *7*, 014002.

(9) Schaibley, J. R.; Yu, H.; Clark, G.; Rivera, P.; Ross, J. S.; Seyler, K. L.; Yao, W.; Xu, X. Valleytronics in 2D materials. *Nature Reviews Materials* **2016**, *1*, 16055.

(10) Massicotte, M.; Schmidt, P.; Vialla, F.; Watanabe, K.; Taniguchi, T.; Tielrooij, K. J.; Koppens, F. H. L. Photo-thermionic effect in vertical graphene heterostructures. *Nat. Commun.* **2016**, *7*, 12174.

(11) Gadelha, A. C.; Cadore, A. R.; Watanabe, K.; Taniguchi, T.; de Paula, A. M.; Malard, L. M.; Lacerda, R. G.; Campos, L. C. Gate-tunable non-volatile photomemory effect in MoS2 transistors. *2D Mater.* **2019**, *6*, 025036.

(12) Lee, C.-H.; Lee, G.-H.; van der Zande, A. M.; Chen, W.; Li, Y.; Han, M.; Cui, X.; Arefe, G.; Nuckolls, C.; Heinz, T. F.; Guo, J.; Hone, J.; Kim, P. Atomically thin p−n junctions with van der Waals heterointerfaces. *Nat. Nanotechnol.* **2014**, *9*, 676−681.

(13) Duan, X.; Wang, C.; Shaw, J. C.; Cheng, R.; Chen, Y.; Li, H.; Wu, X.; Tang, Y.; Zhang, Q.; Pan, A.; Jiang, J.; Yu, R.; Huang, Y.; Duan, X. Lateral epitaxial growth of two-dimensional layered semiconductor heterojunctions. *Nat. Nanotechnol.* **2014**, *9*, 1024−1030.

(14) Kwak, D.-H.; Jeong, M.-H.; Ra, H.-S.; Lee, A.-Y.; Lee, J.-S. Lateral WSe2 p−n Junction Device Electrically Controlled by a Single-Gate Electrode. *Adv. Opt. Mater.* **2019**, *7*, 1900051.

(15) Baugher, B. W. H.; Churchill, H. O. H.; Yang, Y.; Jarillo-Herrero, P. Optoelectronic devices based on electrically tunable p−n diodes in a monolayer dichalcogenide. *Nat. Nanotechnol.* **2014**, *9*, 262−267.

(16) Fukuda, H.; Ohtsu, M. Near-Field Photocurrent Measurements of Si p-n Junction under the Reverse-Bias Condition. *Jpn. J. Appl. Phys.* **2001**, *40*, L286−L288.

(17) Kolb, G.; Obermüller, C.; Karraï, K.; Abstreiter, G.; Böhm, G.; Tränkle, G.; Weimann, G. Photodetector with subwavelength spatial resolution. *Ultramicroscopy* **1995**, *57*, 208−211.

(18) Saito, N.; Sato, F.; Takizawa, K.; ichi Kusano, J.; Okumura, H.; Aida, T.; Saiki, T.; Ohtsu, M. Spatially Resolved Detection of Electroluminescence from Lateral p-n Junctions on GaAs (111)A Patterned Substrates Using a Near-Field Scanning Optical Microscope. *Jpn. J. Appl. Phys.* **1997**, *36*, L896−L898.

(19) Xue, W.; Sahoo, P. K.; Liu, J.; Zong, H.; Lai, X.; Ambardar, S.; Voronine, D. V. Nano-optical imaging of monolayer MoSe2-WSe2 lateral heterostructure with subwavelength domains. *J. Vac. Sci. Technol., A* **2018**, *36*, 05G502.

(20) Berweger, S.; Zhang, H.; Sahoo, P. K.; Kupp, B. M.; Blackburn, J. L.; Miller, E. M.; Wallis, T. M.; Voronine, D. V.; Kabos, P.; Nanayakkara, S. U. Spatially Resolved Persistent Photoconductivity in MoS2−WS2 Lateral Heterostructures. *ACS Nano* **2020**, *14*, 14080−14090.

(21) Hayazawa, N.; Inouye, Y.; Sekkat, Z.; Kawata, S. Metallized tip amplification of near-field Raman scattering. *Opt. Commun.* **2000**, *183*, 333−336.

(22) Stöckle, R. M.; Suh, Y. D.; Deckert, V.; Zenobi, R. Nanoscale chemical analysis by tip-enhanced Raman spectroscopy. *Chem. Phys. Lett.* **2000**, *318*, 131−136.

(23) Blum, C.; et al. Tip-enhanced Raman spectroscopy - An interlaboratory reproducibility and comparison study. *J. Raman Spectrosc.* **2014**, *45*, 22−31.

(24) Novotny, L.; Hecht, B. *Principles of nano-optics*; Cambridge University Press, 2012.

(25) Yang, B.; Chen, G.; Ghafoor, A.; Zhang, Y.; Zhang, Y.; Zhang, Y.; Luo, Y.; Yang, J.; Sandoghdar, V.; Aizpurua, J.; Dong, Z.; Hou, J. G. Sub-nanometre resolution in single-molecule photoluminescence imaging. *Nat. Photonics* **2020**, *14*, 693−699.

(26) Matsui, R.; Verma, P.; Ichimura, T.; Inouye, Y.; Kawata, S. Nanoanalysis of crystalline properties of GaN thin film using tip-enhanced Raman spectroscopy. *Appl. Phys. Lett.* **2007**, *90*, 061906.

(27) Shao, F.; Zenobi, R. Tip-enhanced Raman spectroscopy: principles, practice, and applications to nanospectroscopic imaging of 2D materials. *Anal. Bioanal. Chem.* 2019, 411, 37−61.

(28) Jorio, A.; Cançado, L. G.; Heeg, S.; Novotny, L.; Hartschuh, A. *Handbook of Carbon Nanomaterials*; World Scientific, 2019; pp 175−221.

(29) Vasconcelos, T. L.; Archanjo, B. S.; Oliveira, B. S.; Valaski, R.; Cordeiro, R. C.; Medeiros, H. G.; Rabelo, C.; Ribeiro, A.; Ercius, P.; Achete, C. A.; Jorio, A.; Cançado, L. G. Plasmon-Tunable Tip Pyramids: Monopole Nanoantennas for Near-Field Scanning Optical Microscopy. *Adv. Opt. Mater.* 2018, 6, 1800528.

(30) Rabelo, C.; Miranda, H.; Vasconcelos, T. L.; Cancado, L. G.; Jorio, A. *Tip-enhanced Raman Spectroscopy of Graphene. 2019 4th International Symposium on Instrumentation Systems, Circuits and Transducers (INSCIT)* 2019, 1−6.

(31) Miranda, H.; Rabelo, C.; Vasconcelos, T. L.; Cançado, L. G.; Jorio, A. Optical Properties of Plasmon-Tunable Tip Pyramids for Tip-Enhanced Raman Spectroscopy. *Phys. Status Solidi RRL* 2020, 14, 2000212.

(32) Vasconcelos, T. L.; Archanjo, B. S.; Oliveira, B. S.; Silva, W. F.; Alencar, R. S.; Rabelo, C.; Achete, C. A.; Jorio, A.; Cançado, L. G. Optical Nanoantennas for Tip-Enhanced Raman Spectroscopy. *IEEE J. Sel. Top. Quantum Electron.* 2021, 27, 1−11.

(33) Gadelha, A. C.; et al. Localization of lattice dynamics in low-angle twisted bilayer graphene. *Nature* 2021, 590, 405−409.

(34) Alencar, A. B.; Barboza, A. P. M.; Archanjo, B. S.; Chacham, H.; Neves, B. R. A. Experimental and theoretical investigations of monolayer and few-layer talc. *2D Mater.* 2015, 2, 015004.

(35) Barcelos, I. D.; Cadore, A. R.; Alencar, A. B.; Maia, F. C. B.; Mania, E.; Oliveira, R. F.; Bufon, C. C. B.; Malachias, A.; Freitas, R. O.; Moreira, R. L.; Chacham, H. Infrared Fingerprints of Natural 2D Talc and Plasmon−Phonon Coupling in Graphene−Talc Hetero-structures. *ACS Photonics* 2018, 5, 1912−1918.

(36) Pizzocchero, F.; Gammelgaard, L.; Jessen, B. S.; Caridad, J. M.; Wang, L.; Hone, J.; Boggild, P.; Booth, T. J. The hot pick-up technique for batch assembly of van der Waals heterostructures. *Nat. Commun.* 2016, 7, 11894.

(37) Mania, E.; Alencar, A. B.; Cadore, A. R.; Carvalho, B. R.; Watanabe, K.; Taniguchi, T.; Neves, B. R. A.; Chacham, H.; Campos, L. C. Spontaneous doping on high quality talc-graphene-hBN van der Waals heterostructures. *2D Mater.* 2017, 4, 031008.

(38) Jorio, A.; Saito, R.; Dresselhaus, G.; Dresselhaus, M. S. *Raman Spectroscopy in Graphene Related Systems*; Wiley-VCH Verlag GmbH & Co. KGaA: Weinheim, Germany, 2011.

(39) Dresselhaus, M. S.; Jorio, A.; Hofmann, M.; Dresselhaus, G.; Saito, R. Perspectives on carbon nanotubes and graphene Raman spectroscopy. *Nano Lett.* 2010, 10, 751−758.

(40) Lee, J. E.; Ahn, G.; Shim, J.; Lee, Y. S.; Ryu, S. Optical separation of mechanical strain from charge doping in graphene. *Nat. Commun.* 2012, 3, 1024.

(41) Neumann, C.; Reichardt, S.; Venezuela, P.; Drögeler, M.; Banszerus, L.; Schmitz, M.; Watanabe, K.; Taniguchi, T.; Mauri, F.; Beschoten, B.; Rotkin, S. V.; Stampfer, C. Raman spectroscopy as probe of nanometre-scale strain variations in graphene. *Nat. Commun.* 2015, 6, 8429.

(42) Das, A.; Pisana, S.; Chakraborty, B.; Piscanec, S.; Saha, S. K.; Waghmare, U. V.; Novoselov, K. S.; Krishnamurthy, H. R.; Geim, A. K.; Ferrari, A. C.; Sood, A. K. Monitoring dopants by Raman scattering in an electrochemically top-gated graphene transistor. *Nat. Nanotechnol.* 2008, 3, 210−215.

(43) Beams, R.; Cançado, L. G.; Oh, S.-H.; Jorio, A.; Novotny, L. Spatial Coherence in Near-Field Raman Scattering. *Phys. Rev. Lett.* 2014, 113, 186101.

(44) Cançado, L. G.; Beams, R.; Jorio, A.; Novotny, L. Theory of Spatial Coherence in Near-Field Raman Scattering. *Phys. Rev. X* 2014, 4, 031054.

(45) Cadore, A. Influência De Impurezas Ionizadas E Moléculas Adsorvidas No Mecanismo De Transporte Elétrico De Grafeno. UFMG, 2013, Available at https://repositorio.ufmg.br/bitstream/1843/BUOS-9HSKKV/1/influencia_de_impurezas_ionizadas_e_mol_culas_adsorvidas_no_mecanismo_de__transporte_el_trico_de_grafeno____alisson_r_cadore.pdf.

(46) Wang, H.; Li, C.; Fang, P.; Zhang, Z.; Zhang, J. Z. Synthesis, properties, and optoelectronic applications of two-dimensional MoS2 and MoS2-based heterostructures. *Chem. Soc. Rev.* 2018, 47, 6101−6127.

(47) Mak, K. F.; He, K.; Lee, C.; Lee, G. H.; Hone, J.; Heinz, T. F.; Shan, J. Tightly bound trions in monolayer MoS2. *Nat. Mater.* 2013, 12, 207−211.

(48) He, X.; Li, H.; Zhu, Z.; Dai, Z.; Yang, Y.; Yang, P.; Zhang, Q.; Li, P.; Schwingenschlogl, U.; Zhang, X. Strain engineering in monolayer WS2, MoS2, and the WS2/MoS2 heterostructure. *Appl. Phys. Lett.* 2016, 109, 173105.

(49) Wang, S.; Ukhtary, M. S.; Saito, R. Strain effect on circularly polarized electroluminescence in transition metal dichalcogenides. *Phys. Rev. Research* 2020, 2, 033340.

(50) Bai, Y.; et al. Excitons in strain-induced one-dimensional moiré potentials at transition metal dichalcogenide heterojunctions. *Nat. Mater.* 2020, 19, 1068−1073.

(51) Edelberg, D.; Kumar, H.; Shenoy, V.; Ochoa, H.; Pasupathy, A. N. Tunable strain soliton networks confine electrons in van der Waals materials. *Nat. Phys.* 2020, 16, 1097−1102.

(52) Utama, M. I. B.; et al. A dielectric-defined lateral heterojunction in a monolayer semiconductor. *Nature Electronics* 2019, 2, 60−65.